

Microsphere-Enabled Modular Formation of Miniaturized In Vitro Breast Cancer Models

Weiwei Wang, Li Zhang, Robert O'Dell, Zhuozhuo Yin, Dou Yu, Hexin Chen, JinPing Liu, and Hongjun Wang*

In search of effective therapeutics for breast cancers, establishing physiologically relevant in vitro models is of great benefit to facilitate the clinical translation. Despite extensive progresses, it remains to develop the tumor models maximally recapturing the key pathophysiological attributes of their native counterparts. Therefore, the current study aimed to develop a microsphere-enabled modular approach toward the formation of in vitro breast tumor models with the capability of incorporating various selected cells while retaining spatial organization. Poly (lactic-co-glycolic acid) microspheres (150-200 mm) with tailorable pore size and surface topography are fabricated and used as carriers to respectively lade with breast tumor-associated cells. Culture of cell-laden microspheres assembled within a customized microfluidic chamber allowed to form 3D tumor models with spatially controlled cell distribution. The introduction of endothelial cell-laden microspheres into cancer-cell laden microspheres at different ratios would induce angiogenesis within the culture to yield vascularized tumor. Evaluation of anticancer drugs such as doxorubicin and Cediranib on the tumor models do demonstrate corresponding physiological responses. Clearly, with the ability to modulate microsphere morphology, cell composition and spatial distribution, microsphere-enabled 3D tumor tissue formation offers a high flexibility to satisfy the needs for pathophysiological study, anticancer drug screening or design of personalized treatment.

1. Introduction

Breast cancer, as one of the most commonly diagnosed cancers in women, affects 1 out of 8 women during their lifetime in the United States.^[1] In recognition of the heterogeneity of its subtypes (such as luminal A, luminal B, HER2 subtype, basal phenotype, and triple negative phenotypes, based on the molecular and histopathological variation),^[2] recent efforts have been geared toward the development of formulae specifically targeted to those known subtypes for better treatment precision and efficacy.

In search of effective therapeutics, establishing pathophysiologically relevant in vitro models would be of importance in empowering our capability of truly identifying those potent ones with significant reduction of the preclinical periods. As highlighted in a recent report, ≈95% of new anti-cancer drugs eventually fail in clinical trials despite early indications of their robust efficacy with pre-clinical models.^[3] Traditionally, screening of anticancer drugs primarily involves the use of 2D tumor cell culture in titer plates and in vivo mouse

W. Wang, L. Zhang, Z. Yin, H. Wang Department of Biomedical Engineering Stevens Institute of Technology Hoboken, NJ 07030, USA E-mail: hongjun.wang@stevens.edu L. Zhang, J. Liu

L. Zhang, J. Liu Department of Respiratory Medicine Zhongnan Hospital Wuhan University Wuhan, Hubei 361005, China

L. Zhang, J. Liu

Wuhan, Hubei 361005, China

L. Zhang, J. Liu

Wuhan Clinical Research Center of Minimally Invasive Treatment of Structural Heart Disease

Wuhan, Hubei 361005, China

The ORCID identification number(s) for the author(s) of this article can be found under https://doi.org/10.1002/smll.202307365

DOI: 10.1002/smll.202307365

R. O'Dell Department of Physics Stevens Institute of Technology Hoboken, NJ 07030, USA

D. Tu Research Laboratory of Electronics Massachusetts Institute of Technology Cambridge, MA 02139, USA

H. Chen Department of Biological Sciences University of South Carolina Columbia, SC 29205, USA

H. Wang Semcer Center for Healthcare Innovation Stevens Institute of Technology Hoboken, NJ 07030, USA

H. Wang Department of Chemistry and Chemical Biology Stevens Institute of Technology Hoboken, NJ 07030, USA www.advancedsciencenews.com



www.small-journal.com

xenograft models. 2D cultures advance our understanding of cancer biology; however, they oftentimes fail to capture the heterogeneity of tumors and the complexity of associated native microenvironment.^[4,5] On the other hand, the mouse xenograft models cannot fully represent human responses to therapeutics due to the intrinsic discrepancy of immune systems. [6] Although humanized animals can help to partially resolve this concern, the associated high cost would be an obstacle for wide adoption. In comparison to reductionist monolayer cell culture, cumulative evidence highlights the advantages of cells grown in 3D conditions for anti-cancer agent evaluation and mechanistic understanding, including the possibility of developing oxygen and nutrient gradients, establishing spatially-resolved cell-cell and extracellular matrix (ECM)-cell interactions, investigating nonuniform exposure of cells within a spheroid to drug/compound, understanding different cell proliferation rates throughout a 3D structure, and interrogating the evolution of tumor-specific stromal cells in the tumorous microenvironment.^[7]

To create 3D culture models, several major strategies have been explored, including: 1) spheroid or organoid culture, in which cell aggregates are either cultured in suspension or within a diluted hydrogel, [8] 2) porous scaffold-assisted 3D culture, in which cells are seeded and cultured within a porous scaffold, [9,10] and 3) hydrogel-encapsulated culture, in which cell-laden hydrogel is cast or printed into 3D structures.[11,12] Although all the above approaches do allow to incorporate various subtypes of cancer cells and cancer-associated stromal cells, limitation has been seen in terms of the controllability of cell spatial organization along with the formulation of a pathophysiologically relevant microenvironment. In addition, the lack of essential compositional structures such as the microvasculature in in vitro models indicates their incapacitation as an effective screening modality. As a matter of fact, tumors, either primary or secondary, oftentimes recruit new vasculature for neoplasm. In absence of blood supply, a tumor lump can only grow into a mass of $\approx 10^6$ cells, roughly a 2-mm sphere, [13] in which cell division in the peripheral region is balanced by the necrosis of the core as a result of inadequate nutrition supply. Such tumors, unless secrete hormones, otherwise cause minimal concerns in vivo. Unfortunately, many tumors do induce abnormal microvessel formation via secretion of proangiogenic factors (e.g., basic fibroblast growth factor, transforming growth factor- α , and vascular endothelial growth factor) to nourish tumor growth and increase possible mutations. More importantly, enriched blood vessels would facilitate metastasis.^[14,15] In this regard, inhibition of tumor angiogenesis becomes part of cancer therapeutic intervention, for example, the FDA-approved antiangiogenic drugs including sorafenib (Nexavar), sunitinib (Sutent), pazopanib (Votrient), and everolimus (Afinitor), as well as those angiogenic antagonists under clinical trials.[16-18] In combination with chemotherapy or radiation, these drugs can significantly increase the survival rate.^[19] Among all methods mentioned previously, spheroids are the most commonly used in drug screening due to easy setup. Upon initial aggregation, cells in the aggregates would secrete extracellular matrix (ECM) components and experience intercellular interactions to form compact and stable structures with a gradient decrease of proliferating cells, oxygen levels, and nutrition supplies from the periphery toward the center. As demonstrated, cells in such 3D tumor spheroids exhibit reduced sensitivity to cytotoxic agents such as 5-fluorouracil, cisplatin, or doxorubicin. [20,21] Clearly, spheroid models would be effective to explore the drug resistance of avascular tissues. However, due to the lack of vasculature, it will not allow to study the formation and progression of vascularized tumors and test those anticancer drugs against angiogenesis. To this end, more robust strategies are clearly needed for better control of the spatial organization of cells and effective incorporation of microvasculature and other cancer-associated stroma in the in vitro tissue models while achieving desirable sizes.

Bioprinting, especially the one with multiple printing heads, enables positioning of selected cells within a printed construct.^[12] However, the lack of robust bioink and the difficulty of prolonging cell viability remain to be the bottle neck for its further utility. On the other hand, the emerging strategies such as bottom-up reconstruction^[22–24] and modular tissue engineering^[25] demonstrate to be effective in tissue fabrication with structural and compositional complexity. Taking advantage of bottom-up reconstruction and modular tissue engineering, we therefore explored the use of porous microspheres as cell carriers for individual cells to form the "modules" and then assembly of such cell-laden modules into 3D constructs to form breast cancer models with the flexibility to accommodate cancer cells and stromal cells and incorporate the microvasculature.

Porous microsphere-assisted creation of in vitro breast cancer models may offer multifaceted benefits, including: 1) separate design of microspheres with physicochemical properties tailored for individual cell type, 2) uniform cell distribution within individual microspheres via dynamic cell seeding, 3) flexibility to combine different cell types in the models at desirable ratios by simply mixing the cell-laden microspheres, 4) creation of inter-sphere channels for mass/gas exchange upon the assembly of cell-laden microspheres into 3D constructs, 5) capability of forming arbitrarily shaped constructs via assembly of the cell-laden microspheres in corresponding molds, and 6) spatial organization of cell-laden microspheres in the assembled construct. In addition, such a strategy can be adapted to create other tissue models with a high scale-up potential. As highlighted in Figure 1, the microsphere-enabled modular formation of breast cancer models was realized by: 1) fabrication of poly(lactic-coglycolic acid) (PLGA) microspheres (150-200 µm in diameter) with varying pore sizes (micropores vs. macropores) for different cell types (breast cancer cells, fibroblasts, and endothelial cells), 2) creation of cell-laden microsphere modules populated with respective cells under dynamic cultivation within spinner flasks, 3) assembly of cell-laden microspheres into 3D constructs within a customized microfluidic chamber and formation of tumor tissue models with the presence of vasculature-like structures. With successful establishment of the tumor models, we further evaluated two known therapeutic molecules (i.e., doxorubicin and Cediranib) for their anticancer efficacy. As demonstrated, the engineered tumor models did show the responses correlated with in vivo outcomes. Such a correlation was similarly reported by Perch and Torchilin in the use of cancer spheroid models, [26] confirming the potentials of our tumor models as the platform for anticancer drug testing. Meanwhile, considering the high flexibility to customize the cell types within the tissue model, the models could be potentially used for pathophysiological study or design of personalized treatment.

16136289,0, Downloaded from https://onlinelibrary.wiley.com/doi/10.1002/smll.202307355 by Wuhan University, Wiley Online Library on [28/11/2023]. See the Terms and Conditions (https://onlinelibrary.wiley.com/rems-and-conditions) on Wiley Online Library for rules of use; OA articles are governed by the applicable Creative Commons License

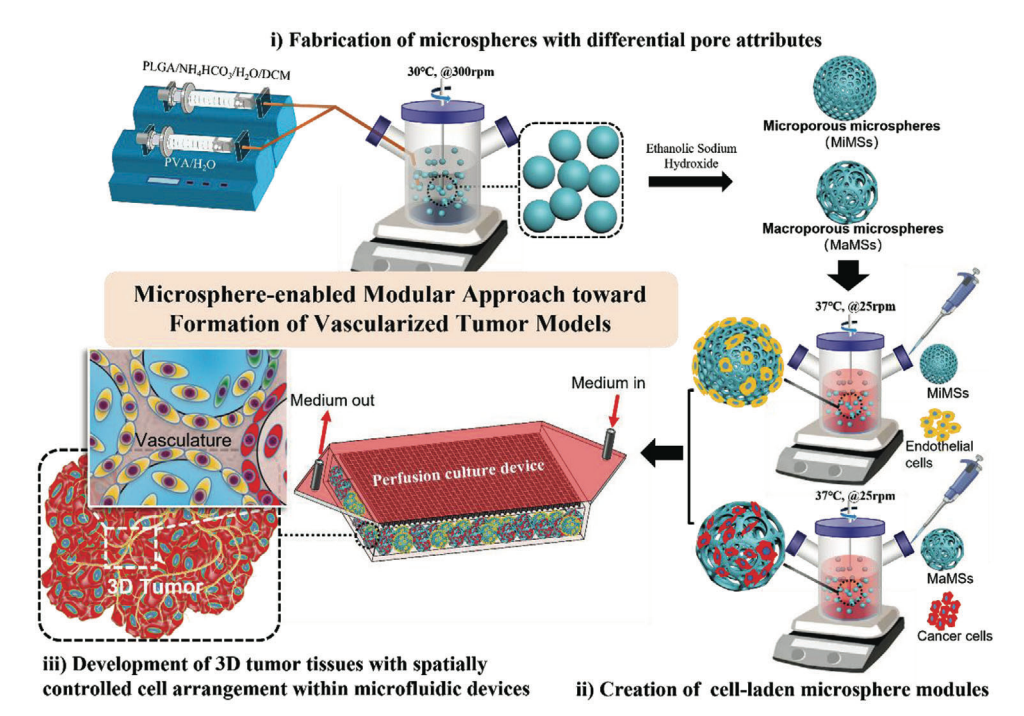


Figure 1. Schematic illustration of the key experimental steps toward the formation of 3D tumor models. Porous PLGA microspheres were fabricated using a double emulsion method and then treated with NaOH-ethanol solution for different times to yield varying pore sizes. Cells were dynamically seeded onto microspheres within spinner flasks and then transferred into microfluidics devices for 3D culture to form tumor models with possible vasculature.

2. Results and Discussion

2.1. Fabrication and Characterization of Porous Microspheres

To fabricate porous PLGA microspheres, the water-oil-water (W-O-W) double emulsion method was adopted with slight modification for better size control as shown in Figure 2A. The diameter of obtained microspheres could be tuned between 50 and 400 µm during the fabrication process by varying several parameters, including PLGA solution concentration, the difference of pumping rate between continuous phase (PVA in H2O) and discontinuous phase (PLGA/NH4HCO3/H2O/DCM), and the stirring speed. In this study, microspheres with a diameter from 100 to 240 µm but mainly at \approx 150–200 µm (Figure 2E) were particularly used as the building blocks to enable the formation of in vitro tumor models simply due to the easiness for pipetting into the microfluidic culture devices. Such sizes were able to accommodate additional pores within the microspheres and yielded sufficient surface areas for cells to attach and spread.[27] To create the pores within PLGA microspheres, NH4HCO3, which decomposed into gaseous NH₃ and CO₂ at the temperature > 30 °C, was used as the porogen. As noted, elevated temperature (e.g., 40 °C vs. 34 °C vs. 25 °C) would be more favorable to form large pores as a result of accelerated gas burst within a unit time. However, at 40 °C less uniform pore formation was noticed. Similarly, increase of water phase would avail more ammonia bicarbonate (in water phase) for decomposition in the unit volume of PLGA, leading to the formation of large pores. Whereas increased W/O ratio caused the instability of the suspension and led to large variation in both pore size and the microsphere size. Upon modulation of temperature (25-40 °C), W/O phase ratio (1:3, 1:1, 2:1), and homogenization method (sonication vs. vortex) (Table S1, Supporting Information), optimal conditions (34 °C, 1:3 W/O ratio and sonication) were established to fabricate porous PLGA microspheres with relatively uniform pores and sphere diameter. Examination of the as-prepared microspheres with the stereomicroscope under backscattered light illumination indeed showed the presence of micropores throughout each sphere (Figure S1A,B, Supporting Information). However, scanning electron microscopic (SEM) imaging of the microsphere surfaces at a low magnification did not show the porous structures clearly and only zoom-in visualization revealed the presence of tiny pores (< 5 µm, Figure 2B-a; Figure S1C, Supporting Information) on the edge of dented areas, which might result from gas eruption of decomposed NH4HCO3. To better examine the pores within the microspheres, both cryo-SEM section and microCT were also conducted to the microspheres. As noted, porous structures were seen throughout the microspheres (Figure 2C-a,D-a). Taken together, the above results suggest that the pores close to the sphere surface are probably sealed by thin PLGA membrane due to the W/O interfacial intension. [28] Considering that ethanol can partially dissolve PLGA, and NaOH can improve the surface wettability of polyesters by facilitating the exposure of carboxylic acid toward the external surface, [28,29] the microspheres were then treated with ethanolic NaOH solution to purposely remove the thin PLGA membrane (≈1 µm thick) for better interconnectivity and larger pore size (Figure S1C, Supporting Information). Depending on the treatment time (1–4.5 min), the surface pore size could be modulated between 5 and 40 µm (Figure 2F), which was evidently confirmed by SEM (Figure 2B; Figure S1C,

16136289, 0, Downloaded from https://onlinelibrary.wiley.com/doi/10.1002/sml.102307365 by Wuhan University, Wiley Online Library on [28/11/2023]. See the Terms and Conditions (https://onlinelibrary.wiley.com/rems-and-conditions) on Wiley Online Library for rules of use; OA articles are governed by the applicable Creative Commons License

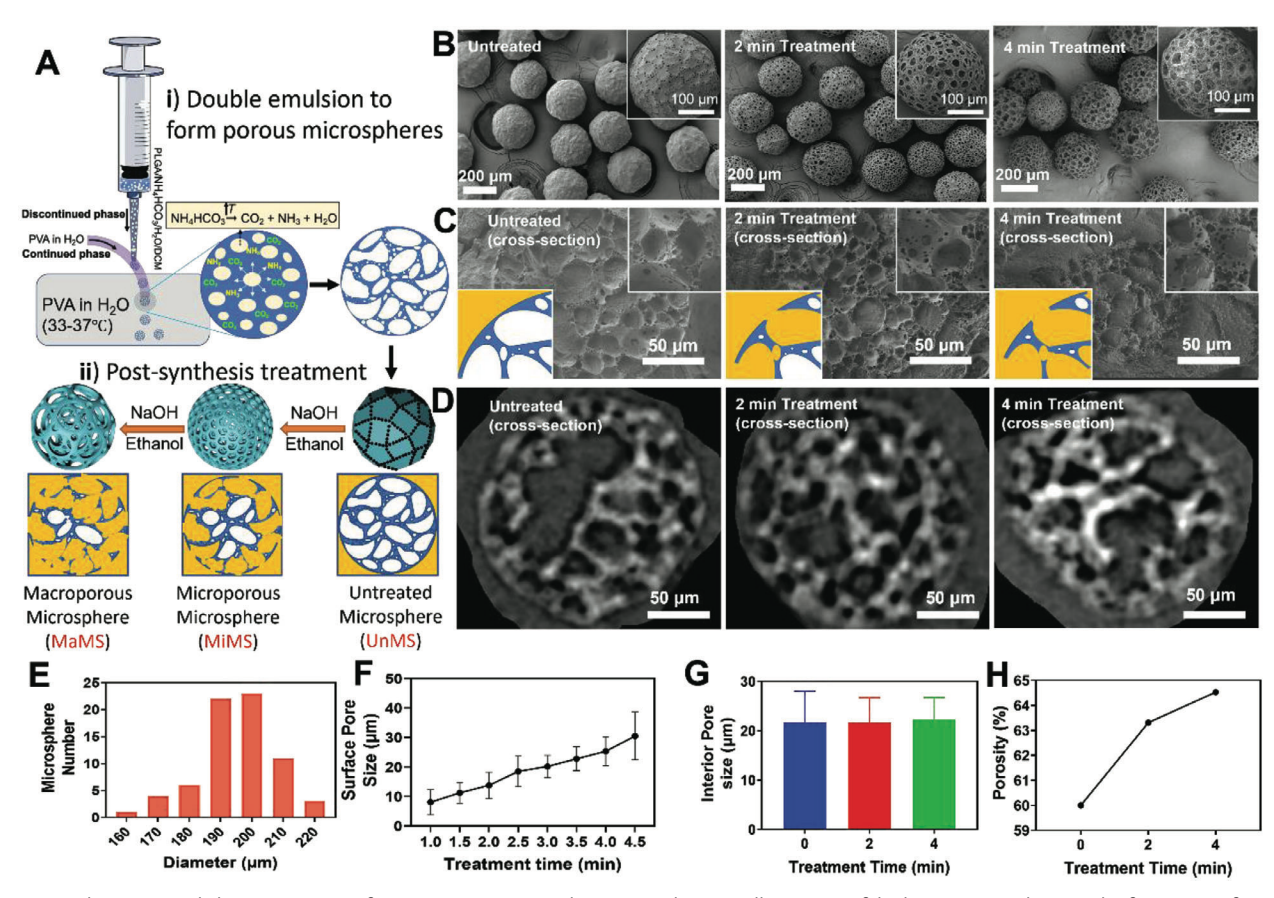


Figure 2. Fabrication and characterization of porous PLGA microspheres. A) Schematic illustration of the key steps involving in the formation of porous microspheres. B) Representative SEM images of microspheres upon various post-synthesis treatments. Insets: Zoom-in images of selected microspheres. C) Representative cryo-SEM images of transverse sections of microspheres upon various post-synthesis treatments. Upper insets: Zoom-in images of selected region. Bottom insets: Schematic illustration of the formation of interconnected pores. D) Representative microCT images of transverse sections of microspheres upon various post-synthesis treatments. E) Diameter distribution of as-prepared microspheres. F) Average surface pore size of microspheres upon various post-synthesis treatments. G) Average interior pore size of microspheres upon various post-synthesis treatments. H) Porosity of microspheres upon various post-synthesis treatments.

Supporting Information). Notably, with the increase of treatment time, the pores on the microsphere surface gradually enlarged until merged into larger pores, however continuous fusion of pores led to the loss of the spherical shape of microspheres and eventually the structural dissociation (≥ 5 min) (Figure S2, Supporting Information). To better maintain the structural integrity with uniform pores, the treatment time was preferably kept within 4 min. Possible changes of interior pores in terms of morphology, size and interconnectivity upon ethanolic NaOH treatment were further examined via cryo-SEM section and microCT. As shown in Figure 2C,D, the size and shape of interior pores remained comparable before and after NaOH treatment despite more interconnecting pores between the main pores (see the insets of illustration and zoom-in SEM). Based on the microCT measurement, the size of interior main pores kept almost unchanged (see Figure 2G). On the other hand, a slight increase of the porosity (non-treated: 60% vs. 4 min treated: 65%, Figure 2H) was noticed, indicating the efficiency of ethanolic NaOH in removal of those inter-pore thin membranes for better interconnectivity. However, with the treatment time further increased, the pore wall became much thinner, and those small pores embedded in the wall got exposed and opened. As such, we can reasonably speculate that both the thinning of inside pore wall and the merging of surface pores cause the collapse of microspheres upon prolonged NaOH/ethanol treatment (see the start of collapse at 4.5 min treatment, Figure S1C, Supporting information).

2.2. Cell Seeding and Culture onto Microspheres to Form Cell-Laden Modules

To achieve even cell distribution among microspheres and better load the cells in the interior pores, cell seeding onto microspheres was performed dynamically within a spinner flask^[30] (Figure 3A), in which microspheres and cells suspended in the stirring media would have equal opportunities to interact and consequently achieve more uniform cell adhesion onto microspheres (as evidenced in Figure S3, Supporting Information). To assure maximum cell-microsphere interactions while avoiding potential damage by media flow-induced shear stress, the stirring speed used for each type of cells was particularly

16136289,0, Downloaded from https://onlinelibrary.wiley.com/doi/10.1002/smll.202307355 by Wuhan University, Wiley Online Library on [28/11/2023]. See the Terms and Conditions (https://onlinelibrary.wiley.com/rems-and-conditions) on Wiley Online Library for rules of use; OA articles are governed by the applicable Creative Commons License

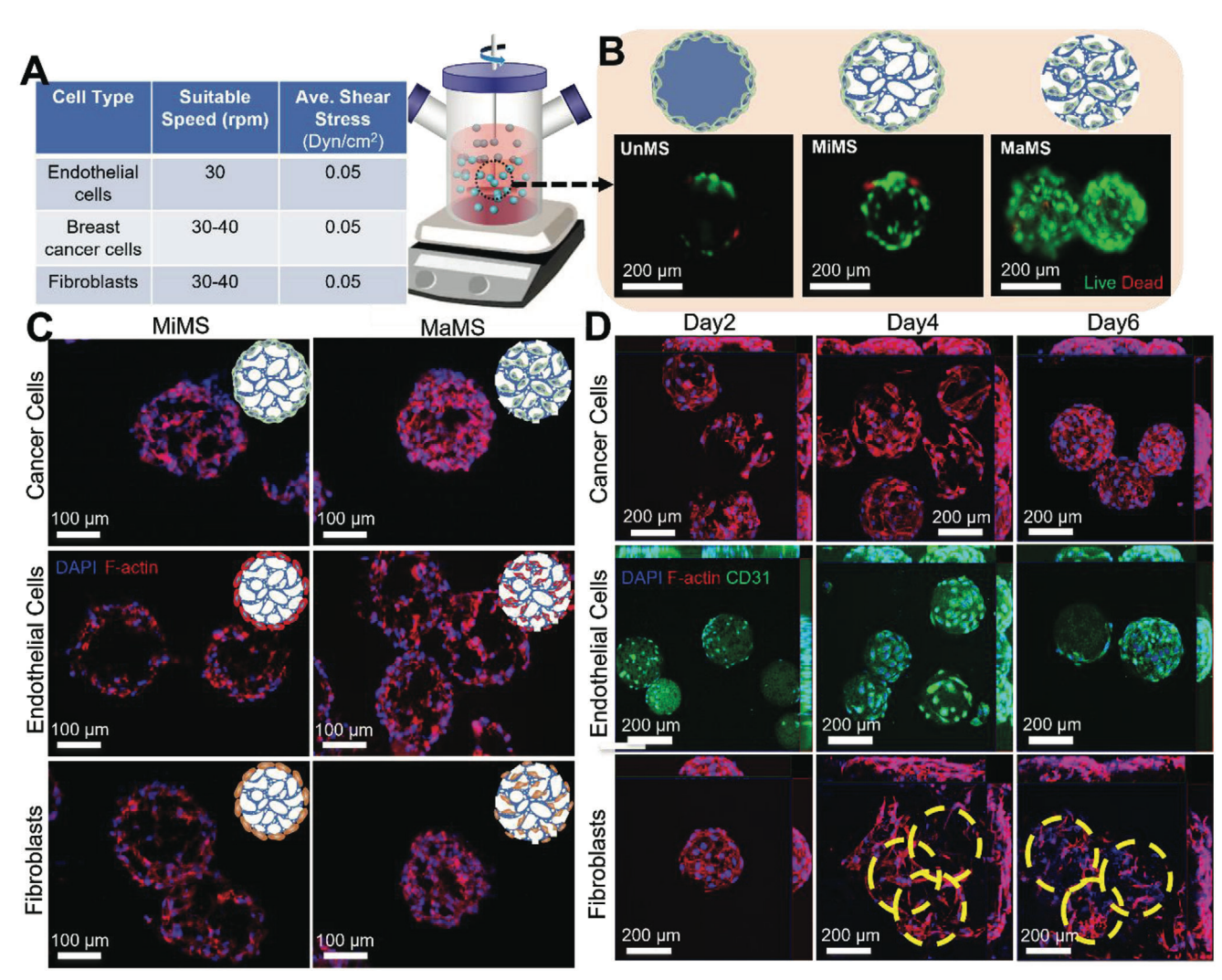


Figure 3. Seeding and culture of cells onto the microspheres with various pores. A) Schematic illustration of dynamic seeding and culture of cells onto microspheres within a spinner flask at the designated stirring speed. B) Fluorescent images of cancer cells dynamically seeded and cultured on various microspheres for 24 h. Cells were stained for live (green) with Calcein AM and dead (red) with Ethidium homodimer-1. C) Fluorescent images of the cross sections of microspheres after culture with respective cells (cancer cells, endothelial cells, and fibroblasts) for 3 days. Cells were stained for F-actin with TRITC-conjugated phalloidin and nuclei with DAPI. D) Confocal images of cell-laden microspheres after culture for different periods. Cells were stained for F-actin with TRITC-conjugated phalloidin and nuclei with DAPI. Endothelial cells were stained with FITC-conjugated anti-CD31 antibody. The yellow circles indicated microspheres that formed aggregations.

chosen based on theoretical calculation and experimental optimization (see Figure 3A). The pore size and pore interconnectivity in microspheres would lead to distinguished spatial distribution of cells within the microspheres. In this regard, three types of microspheres with distinct pore interconnectivity, *i.e.*, microspheres without ethanolic NaOH treatment (referred as UnMS, surface pore size <5 μ m), microspheres with 2-min ethanolic NaOH treatment (referred as MiMS, surface pore size: $12 \pm 3 \mu$ m) and microspheres with 4-min ethanolic NaOH treatment (referred as MaMS, surface pore size: $25 \pm 6 \mu$ m), were first explored for seeding with MDA-MB-231 cells. As shown in Figure 3B, after dynamic seeding for 24 h, cells (green fluorescence) attached onto the UnMS surface were limited while more cells were clearly seen on the MiMS and MaMS microspheres with relatively uniform cell distribution across the surface, implicating the prefer-

ence of cell attachment onto porous microspheres. Meanwhile, a high cell viability (> 90%, Figure 3B) was detected on all cell-laden microspheres, indicating the appropriateness of the stirring speed (40 rpm) for seeding of MDA-MB-231 cells onto microspheres. The adhesion percentages of cells to these three types of microspheres also showed that MaMS yield the largest cell coverage, followed by MiMS, and UnMS the least (Figure S4, Supporting Information). Both MaMS and MiMS supported cell attachment, but the larger pores of MaMS would ease the cellular access to interior surface of pores for cell growth and nutrient infiltration. To confirm such an assumption, MiMS and MaMS were respectively seeded and cultured with cancer cells (MDA-MB-231), endothelial cells (MS-1) and fibroblasts (normal human dermal fibroblasts, NHDF) for 3 days. Upon dynamic seeding for 24 h, uniform cell attachment to the microsphere

16136289, 0, Downloaded from https://onlinelibrary.wiley.com/doi/10.1002/sml.102307365 by Wuhan University, Wiley Online Library on [28/11/2023]. See the Terms and Conditions (https://onlinelibrary.wiley.com/rems-and-conditions) on Wiley Online Library for rules of use; OA articles are governed by the applicable Creative Commons License

surface was observed for all three types of cells (data not shown). Fluorescent staining of the cross-sections of 3-day cell-laden microspheres revealed differential cell distribution with MiMS and MaMS (Figure 3C). Overall, the rough surface of MiMS provided enough anchorage for cells to attach to; however, the small pore size did not encourage the infiltration of cells into the interior space. MaMS, on the other hand, not only provided the cells with anchorage over the surface but also allowed for cell infiltration throughout the microspheres. As noted, breast cancer cells and fibroblasts occupied almost all the space inside MaMS while endothelial grew confluently on the MiMS surface and infiltrated only to the superficial region, which was similarly observed with MaMS despite slightly more cells inside the spheres. Moreover, immunofluorescent staining for intercellular junction protein, i.e., PECAM-1 (CD-31), showed MiMS better supported the development of intercellular junctions on MiMS (Figure S5, Supporting Information), implying its benefits for endothelial cells to form the endothelial layers on the 2D anchorage surface, consistent with previous findings.^[31] Such an intercellular integrity of endothelial cells on MiMS surface would favor and facilitate the formation of a vascular network among the inter-microsphere space upon assembly of cell-laden microspheres within the microfluidic chamber (Figure 1-iii). Serving as the modules for assembly into 3D tissue constructs, timeresolved proliferation (2, 4 and 6 days) of respective cells on corresponding microspheres, i.e., breast cancer cells and fibroblasts on MaMS and endothelial cells on MiMS, was investigated to determine the optimal culture time prior to the transfer into the microfluidic chamber for assembly. In order to assemble all cell-laden microspheres in the perfusion chamber, the cell-laden microspheres were required to be capable of individually suspended in culture media. However, some cells (fibroblasts) tend to form aggregates earlier, which makes it difficult to transfer via pipetting. Thus, culturing different types of cells onto the preferred microspheres for cell coverage will allow us to determine the proper time to collect cell-laden microspheres and then transfer them to the perfusion device. CellTiter Blue proliferation assay (Figure S6, Supporting Information) confirmed that all three types of cells continuously increased their metabolic activity during the 6-day dynamic culture period; however, differential cell behaviors were also noticed. As shown in confocal microscopic observations of the cell-laden microspheres (Figure 3D) and histological analysis of the cross-sections of cell-laden microspheres (Figure S7, Supporting Information), MDA-MB-231 cells were able to continuously grow and fill the surface and interior pores of MaMS during the 6-day culture. In contrast, endothelial cells on MiMS could cover the entire surface of microspheres by day 6 and develop intercellular junctions (Figure S5, Supporting Information); beyond that time the cells became unhealthy based on the live/dead staining (Figure S8, Supporting Information). Compared to cancer cells (MDA-MB-231 cells), fibroblasts (NHDF) with larger spreading area quickly attached to the MaMS and occupied the pores within 2 days (Figure 3D; Figure S7, Supporting Information). However, upon extended culture fibroblasts had a high tendency to reach out to the neighboring cell-laden MaMS and form aggregates (Figure 3D; Figure S7, Supporting Information), causing the difficulty of transferring via pipetting and evenly mixing with other cell-laden microspheres. Based on the above observations, the optimal

dynamic culture duration for individual cells on microspheres prior to assembly would be: 6 days for cancer cells on MaMS, 6 days for endothelial cells on MiMS, and 2 days for fibroblasts on MaMS.

2.3. Microfluidic Culture Platform Design and Optimization

To better support the assembly of cell-laden microspheres into 3D tumorous tissues while retaining spatially controlled distribution of various cells, a microfluidic culture platform was accordingly designed, comprising two chambers (upper media chamber and bottom culture chamber) separated by a 70-um-thick, porous nylon mesh (pore size: ≈70 µm) (Figure 4). The culture chamber [3 mm (w) \times 4 mm (l) \times 1 mm (d)] was large enough to support the assembly of multilayers of cell-laden microspheres while the media chamber [5.5 mm (w) \times 7.5 mm (l) \times 0.15 mm (d)] primarily accommodated the media flow (emulate the function of arterioles) and allowed the nutrients and oxygen to infiltrate the culture chamber with reduced shear stress (see the shear stress distribution in computational simulation, Figure 4B). The nylon mesh constrained cell-laden microspheres within the culture chamber while allowing for free exchange of nutrition/waste through the large pores between the culture chamber and media chamber. Different media flow rates were also investigated to understand the media flow pattern and shear stress throughout the chambers (Figure 4C). As identified, the flow rate at 0.15 mL h⁻¹ offered uniform media distribution and might be sufficient to provide nutrition to the assembled cells. Furthermore, in the early stage of assembled cell-laden microspheres in the culture chamber, media would flow through the gaps/pores between/within the porous microspheres for nutrition delivery to cells, which was demonstrated in the COMSOL simulation (Figure 4C stage 0). Gradually when the void space was filled with proliferated cells and newly formed tissue, media was more shunted through the upper media chamber, which can effectively divert shear stressinduced destruction from newly formed tissues (Figure 4C stage 2) and at this stage the nutrition supply would primarily rely on diffusion. Figure 5 did show the time-dependent formation of 3D tissue from cell-laden microspheres (MS-1-laden MiMS and MDA-MB-231-laden MaMS at 1:1 ratio). Immunofluorescent staining of MS-1 for CD-31 (green) showed an increase in fluorescently positive cells in the cultured structure, suggesting the occurrence of continuous cell growth within the culture chamber (Figure 5A). As a matter of fact, such microfluidic culture conditions are notably beneficial to support cell growth even for those cells laden onto solid microspheres (Figure S9, Supporting Information), which were recognized for the limited surface area unfavorable for cell anchorage and subsequent formation of interconnected tissue constructs. As a result, an integrated 3D tissue formation was expected from the cell-laden porous microspheres. In contrast to still disaggregated cell-laden microspheres at day 7, an integrated 3D structure was indeed formed after culture for 10 days or longer (Figure 5A-i vs. ii). This was evidently demonstrated with 10-day cultured constructs upon staining with methylene blue (Figure 5B-i,ii), retaining its structural integrity even after extraction from the culture chamber despite the possibility of still recognizing individual microspheres. The 14-day proliferation curve of cells in the perfusion chamber also

www.small-journal.com

16136289,0, Downloaded from https://onlinelibrary.wiley.com/doi/10.1002/smll.202307355 by Wuhan University, Wiley Online Library on [28/11/2023]. See the Terms and Conditions (https://onlinelibrary.wiley.com/rems-and-conditions) on Wiley Online Library for rules of use; OA articles are governed by the applicable Creative Commons License

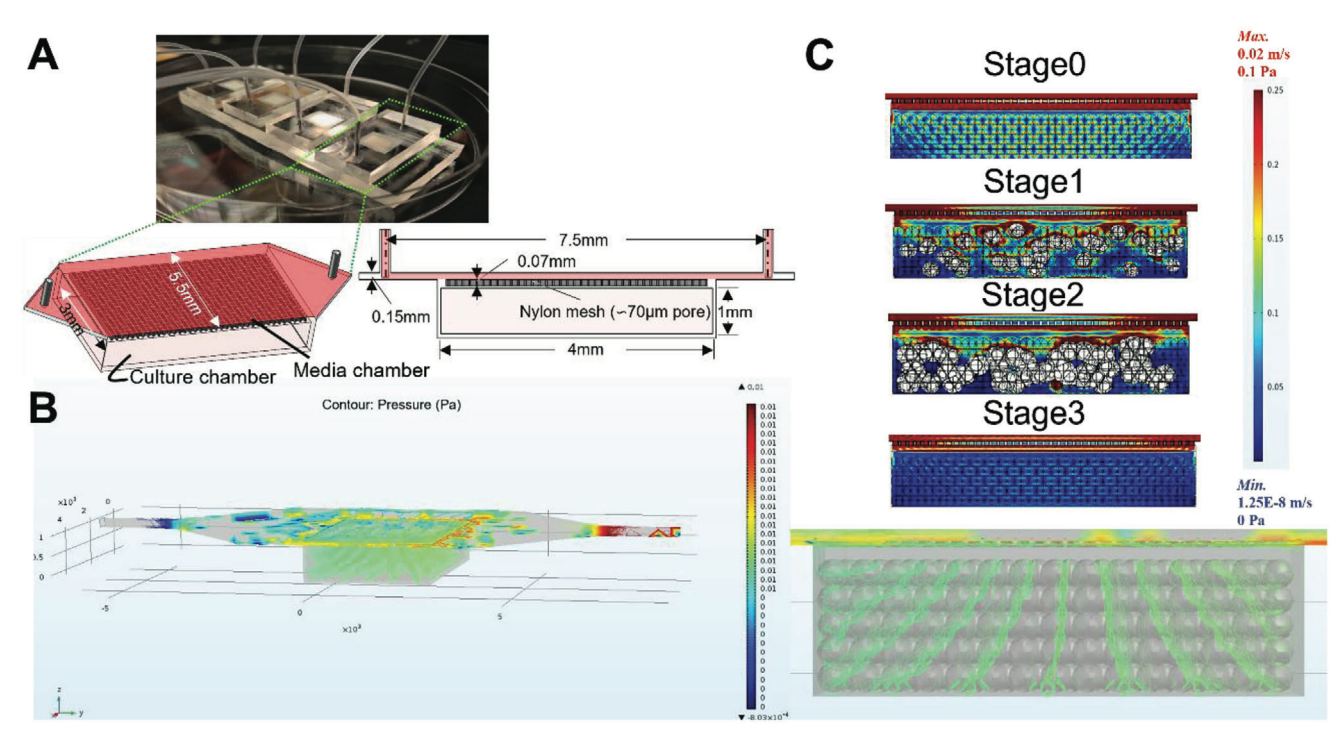


Figure 4. Dual-chamber microfluidic culture platform accommodating the formation of tumor tissue from cell-laden microsphere modules. A) Design and dimensions of a dual chamber microfluidic device with an upper media chamber and a bottom culture chamber, which is separated by the porous nylon mesh. B) Distribution of pressurized media throughout assembled microspheres within the microfluidic device as simulated by fluid dynamics of COMSOL (left) and zoom-in side view (right). C) Simulation results with four different stages of cell growth/tissue formation among microspheres. White color areas indicated randomized cell growth/tissue formation between microspheres in stage 1 and 2.

indicated that starting from day 7, the cells in the chamber were undergoing rapid growth (Figure S10, Supporting Information). Staining the transverse sections of the culture with hematoxylin and eosin (H&E) revealed the presence of both MiMS and MaMS roughly at a 1:1 ratio (Figure 5B-iii). Obviously, continuous cell proliferation and new ECM synthesis during the culture helped to fill the inter-sphere space and bridge the neighboring cellladen microspheres to form one integrated piece. As noted, a majority of cells within the cultured constructs remained alive (data not shown) after culture for 14 days, suggesting efficient nutrition supply through assembled cell-laden microspheres via inter-microsphere space or the small pores of MiMS during the culture period. Further analysis of the stained sections confirmed the primary distribution of cells on the surface of MiMS while more cells within MaMS, and meanwhile the cell-laden microspheres were connected (Figure 5B-iii).

To explore the possibility of spatially controlling the organization of various cell-laden microspheres during the assembly, MS-1 and MDA-MB-231-laden microspheres were used as representative modules for assembly. As shown in the insets of Figure 5C, different assembly scenarios were tested. In the random assembly (Figure 5C-i-iii), MS-1- and MDA-MB-231-laden microspheres at different ratios (3:1, 1:1 or 1:3) were gently mixed and then transferred to the culture chamber. In the layering assembly (Figure 5C-iv,v), either MS-1 or MDA-MB-231-laden microspheres were first transferred to the culture chamber and then the same amount of MDA-MB-231 or MS-1-laden microspheres were added on the top. In the side-by-side assembly, a divider was temporarily inserted into the culture chamber to separate the microspheres laden with different cells during the assembly. Immunofluorescent staining of the cross-sections of 10-day culture assembly did show the spatial distribution of corresponding cells following the initial arrangement, confirming the capability of spatially controlling cell distribution in microsphere-enabled cell assembly into 3D constructs. Apparently, compared to those cultures to form tumorous tissues by seeding the cancer cells onto preformed scaffolds,[32,33] the use of cell-laden microspheres as modules for assembly provides the flexibility to customize the composition of each type of modules, while achieving desirable spatial organization to better accommodate the complexity of native tissues.[34]

2.4. Formation of Tumor-Like 3D Tissue Constructs from Cell-Laden Modules

To maximally recapitulate the key cellular components of native tumor, mainly composed of stromal cells and cancer cells, MDA-MB-231-laden MaMS, NHDF-laden MaMS and MS-1 cellladen MiMS at a ratio of 2:1:2 were mixed and then assembled within the culture chamber of microfluidic devices and cultured for 10 days. The presence of fibroblasts and endothelial cells would encourage the development of 3D tumor tissues with the presence of vasculature networks and cancerassociated fibroblasts.[35,36] Upon culture for 10 days within the culture chamber, cell-laden microspheres were fused into an

16136289,0, Downloaded from https://onlinelibrary.wiley.com/doi/10.1002/smll.202307355 by Wuhan University, Wiley Online Library on [28/11/2023]. See the Terms and Conditions (https://onlinelibrary.wiley.com/rems-and-conditions) on Wiley Online Library for rules of use; OA articles are governed by the applicable Creative Commons License

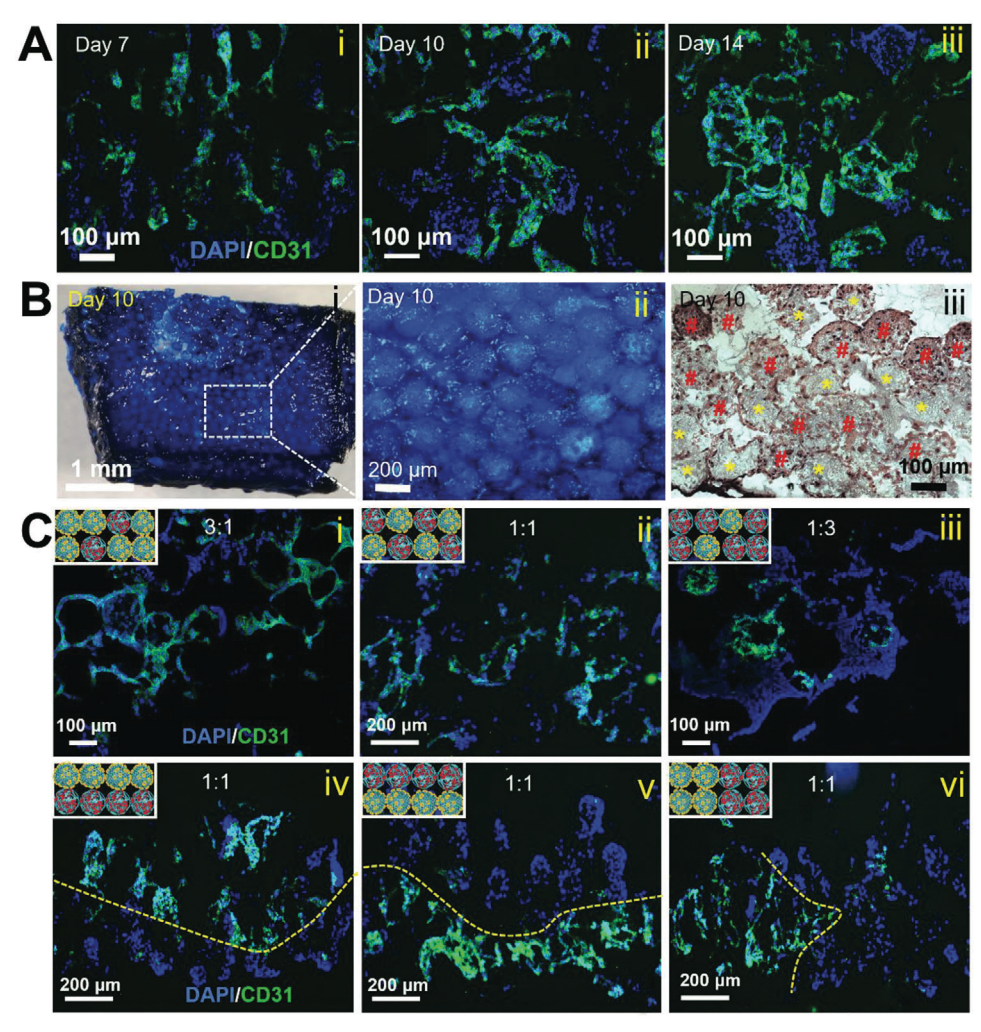


Figure 5. Temporospatial control of tissue formation via the assembly of cell-laden microsphere modules (MS-1-laden MiMS and MDA-MB-231-laden MaMS) within the microfluidic culture chamber. A) Time-dependent tissue formation of the assembled cell-laden microspheres (MS-1/MiMS and MDA-MB-231/MaMS at 1:1) for 7 i), 10 ii) and 14 iii) days. Frozen sections were immunofluorescently stained for CD31 (green) and nuclei (blue) with DAPI. B) Stereomicroscopic images i and ii) and light microscopic image iii) of the cultured constructs of cell-laden microspheres after 10 days. The harvested tissue block was either stained with 1% methylene blue i and ii) or embedded in paraffin to obtain thin cross-sections for hematoxylin and eosin staining iii). * Denotes MiMS; # denotes MaMS. C) Tissue formation of the assembled cell-laden microspheres by day 10 at different ratios (MS-1/MiMS: MDA-MB-231/MaMS = 3:1 i), 1:1 ii), and 1:3 iii)) or with different spatial distribution (MS-1/MiMS on the top iv), on bottom v), and on the left vi)).

integrated structure as evidenced by the H&E-stained crosssections (Figure 6A). Immunofluorescence staining of the crosssections of the cultures for α -smooth muscle actin (α -SMA) (Figure 6B), a known marker for cancer-associated fibroblasts (CAF),[37] revealed the presence of CAFs among cancer cell clumps, implying that cytokines like transforming growth factor (TGF)- β 1 secreted by cancer cells could induce the fibroblast-to-CAF conversion in a similar fashion to in vivo circumstances.^[38] Cumulative evidence has shown that loss of E-cadherin, expressed on the epithelial cell membrane for adhesion, [39] is often associated with the epithelial-mesenchymal transition of cancer cells, which is responsible for metastasis. In this regard, crosssections of the culture were also immunofluorescent stained for E-cadherin. As shown in Figure 6C, limited cancer cells were stained positively for E-cadherin, while most of them had a faint or no staining, affirming the invasive and poorly differentiated characteristics of MDA-MB-231 cells. Besides, we also carefully investigated vascularization occurred within co-cultured assemblies. Several scenarios (Figure 7A schematic illustrations) were identified toward the possible establishment of vasculature networks within the assembled tumor-like tissue during coculture. As shown in Figure 7A, endothelial cells on the surface of microspheres could either organize into vascular-like structure with an open lumen (indicated by arrow heads) following the inter-microsphere tortuous path (Figure 7A-i), branch out to form a network with neighboring endothelial cells in the intermicrosphere space (Figure 7A-ii), branch inwards to develop the network of smaller diameter (≈8 μm) along the interior pores of MiMS (Figure 7A-iii), or sprout out to reach the adjacent MaMS (Figure 7A-iv) while MDA-MB-231 cells in MaMS would infiltrate MiMS (Figure 7A-v). Notably, sprouting angiogenesis seemingly dominated the vascularization process. To better

16136289, 0, Downloaded from https://onlinelibrary.wiley.com/doi/10.1002/sml1.202307365 by Wuhan University, Wiley Online Library on [28/11/2023]. See the Terms and Conditions (https://onlinelibrary.wiley.com/ems-and-conditions) on Wiley Online Library for rules of use; OA articles are governed by the applicable Cectaive Commons Licesea.

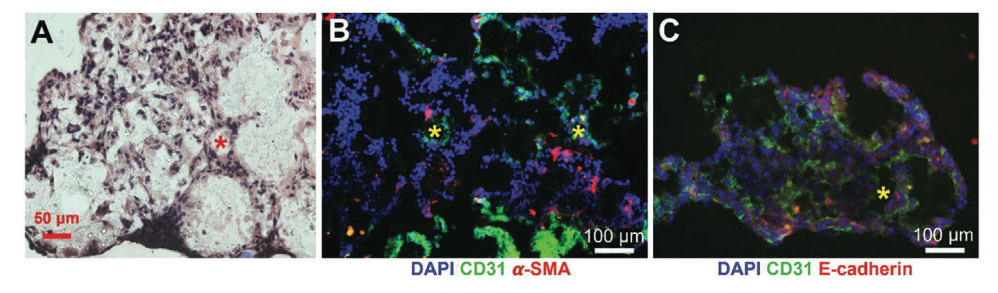


Figure 6. Representative fluorescence images of 10-day cultured cell-laden microspheres containing MDA-MB-231 cells, MS-1 cells and NHDFs at a ratio of 2:2:1. Cross-sections were stained with H&E for histology A) or immunofluorescently stained for CD-31 (green), α -smooth muscle actin (α -SMA) (red) and nuclei (blue) B) or CD-31 (green), E-cadherin (red) and nuclei (blue) C). * Indicates the presence of endothelialized tubular structure.

understand the process, immunofluorescently stained thick tissue sections (≈30 µm) were examined under the laser scanning confocal microscope. As noted, sprouting was seen from the surface of MiMS covered with confluent endothelial cells (with intercellular junctions established, Figure 7B inset) and invaded the neighboring cancer cell clumps to form vascular networks (Figure 7B; Figure S11, Supporting Information). As a matter of fact, the process of sprouting involves complex yet highly coordinated and dynamic interactions between endothelial cells and their microenvironment. During sprouting, pro-angiogenic signals (such as vascular endothelial growth factor (VEGF)-A) secreted by MDA-MB-231 cells^[40] promote proliferation of

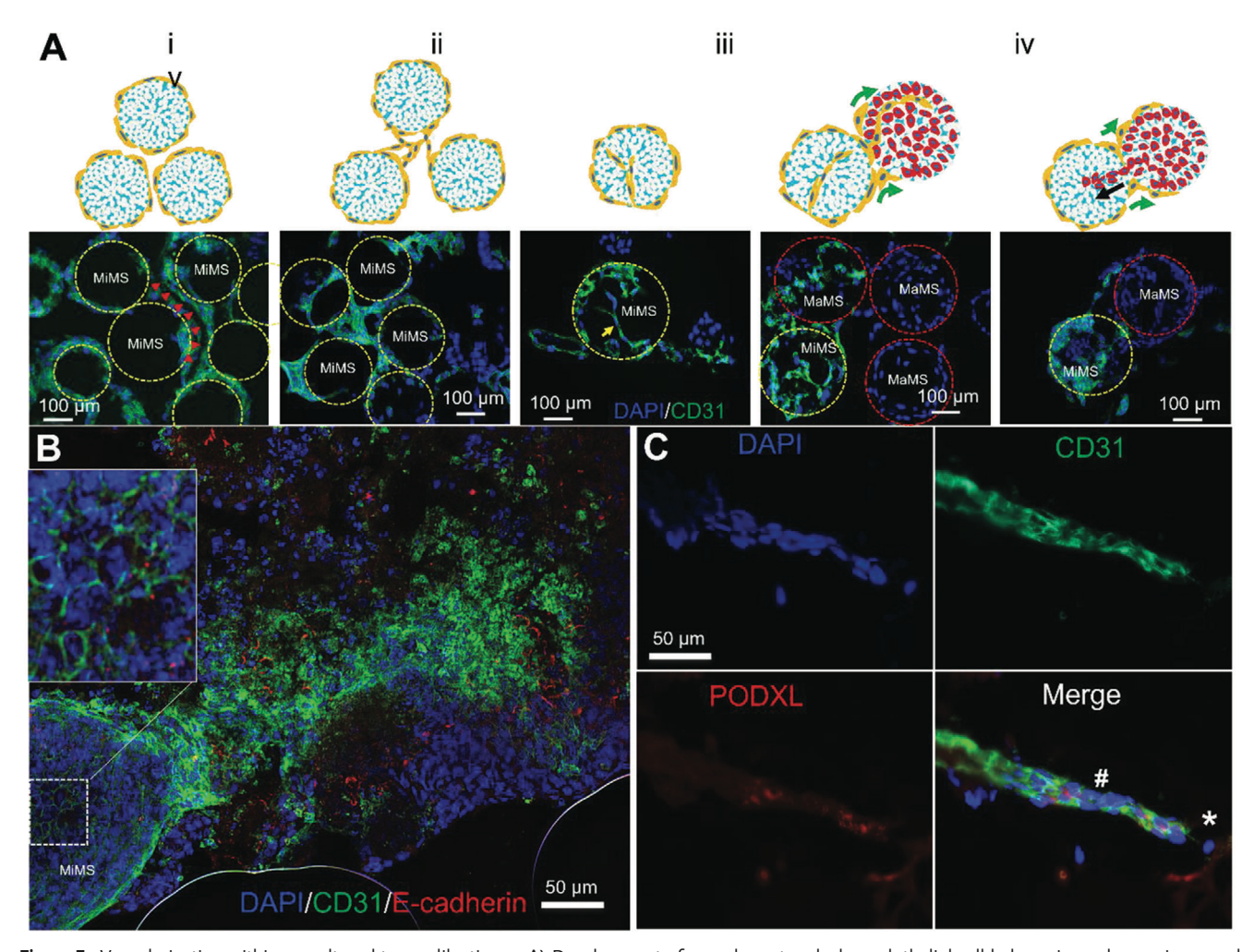


Figure 7. Vascularization within co-cultured tumor-like tissue. A) Development of vascular networks by endothelial cell-laden microspheres via several representative scenarios. B) Confocal image to show the sprouting of endothelial cells from MiMS into surrounding cancer cell aggregates. Inset: zoomin image of intercellular junctions. C) Representative fluorescent image to show the possible tip cells (*) and stalk cells (#) of a typical sprouting vessel, in which frozen sections were stained for CD31 (green) and PODXL (red).

16136289, 0, Downloaded from https://onlinelibrary.wiley.com/doi/10.1002/sml.102307365 by Wuhan University, Wiley Online Library on [28/11/2023]. See the Terms and Conditions (https://onlinelibrary.wiley.com/rems-and-conditions) on Wiley Online Library for rules of use; OA articles are governed by the applicable Creative Commons License

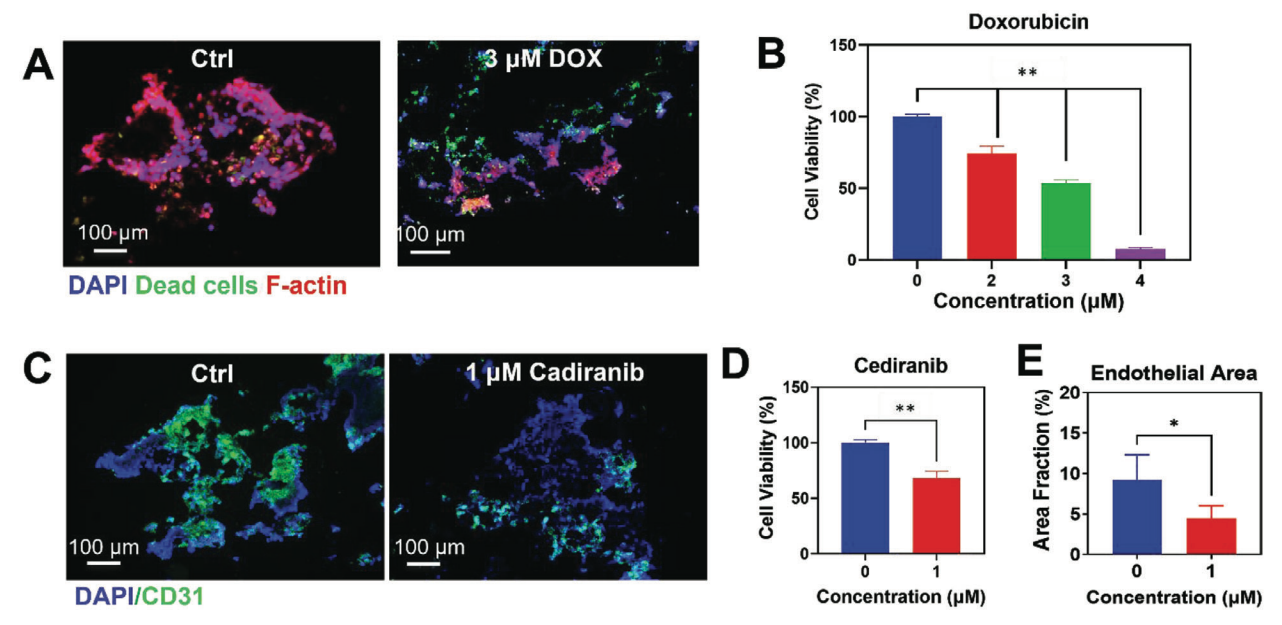


Figure 8. Drug testing on the 3D tumor models. A) Representative florescence images of tumor tissue upon treatment without (left, control) or with 3 μm doxorubicin (DOX) for 48 h. B) Cell viability measurement upon treatment with DOX of different concentrations (0, 2, 3, and 4 μm) for 48 h. C) Representative florescence images of tumor tissue upon treatment without (left, control) or with 1 μm Cediranib for 48 h. D) Cell viability measurement upon treatment without or with 1 μm Cediranib for 48 h. E) Semi-quantification of endothelial area (CD-31 positive cells) of the tumor tissue treated without or with 1 μm Cediranib for 48 h. * p<0.05, *** p<0.01. n = 5.

endothelial cells and their subsequent motility and filopodia extension, and through notch signaling regulate the development of tip cells and stalk cells for directional formation of new vascular structure (Figure 7C), which either wrapped around or invaded the cancer/fibroblast cell-laden MaMS (Figure S11B, Supporting Information). As noted, the tubular structures (Figure 7A red arrows) had a diameter of $\approx 10 \mu m$, close to the size of those capillaries (\approx 5 to 10 μm) seen in the human tumor tissue.^[41,42] Actually, cancer cells are closely associated with our vascular system, i.e., promoting abnormal angiogenesis for oxygen and nutrient while relying on the permeable vasculature network for metastasis.[43-46] To further determine the sprouting in the culture chamber is not a random behavior of endothelial cells, immunofluorescence staining for podocalyxin (PODXL), a CD34related sialomucin regulating cell adhesion, migration, and polarity, was conducted to the frozen sections of the culture. In general, only polarized endothelial cells that undergo pathological pre-angiogenesis would be PODXL positive, otherwise they are not.[47] As shown in Figure 7C, the endothelial cells in the sprouting branch were indeed stained positively for PODXL, indicating that these endothelial cells are committed toward angiogenesis. Interestingly, a close examination of the staining also revealed the possible presence of tip cells and stalk cells in the sprouting.

2.5. Utility of Tumor-Like 3D Tissue Constructs for Drug Testing

One of the immediate applications of the established in vitro tumor models can be used for drug testing/screening in anticipation of some similar responses to the in vivo circumstances. In view of the high flexibility to customize the cellular composition of tumor tissue with the current platform, we started with

a simplified breast tumor model established with MDA-MB-231 cell-laden MaMS and fibroblast-laden MaMS to test a generic yet efficient anticancer drug, i.e., doxorubicin (DOX), demonstrated for its efficacy in treating breast cancer. [48] Through the chamber with co-culture of 1:2 NHDF/MaMS and MDA-MB-231/MaMS after 10 days was DOX solution at different concentrations (0, 2, 3 and 4 μ M) in culture media perfused via the inlet for 48 h. As shown in Figure 8A, examination of the cross-sections of cultures infused with the Zombie Aqua fixable viability kit revealed a large portion of cells in the culture treated with 3 µM DOX for 48 h were killed (green fluorescence). In comparison, only a small area of green fluorescence was seen with 2 μ M DOX, while no viable cells were seen with 4 µM DOX treatment (Figure S12, Supporting Information). As expected, very limited cell death was observed with nontreated controls. To better quantify the anticancer efficacy of DOX on the tissue model, Cell TiterBlue-based cell viability assay was conducted on the culture (Figure 8B). Consistent with the findings from Zombie Aqua analysis, treatment with 4 μM DOX displayed a minimum cell viability (negligible cell survival after 48 h), suggesting this concentration might be too high. Interestingly, treatment with 2 µM DOX only yielded less than 20 ± 5% inhibitory efficacy in comparison to nontreated controls, implying such a concentration might not be enough to show the anti-cancer effect.^[49,50] On the other hand, treatment with 3 µM DOX did lead to $53 \pm 2\%$ cancer inhibition in comparison to non-treated controls, indicating the IC50 for the currently established tissue model is 3 µM, much higher than the IC50 for 2D culture (87.7 \pm 10.6 nM) or for MDA-MB-231 spheroid culture (636.0 \pm 160.3 nM^[51]) with comparable drugging period. Such a noticeable disparity in IC50 might result from a larger size of the tumor model than typical spheroids (e.g., \approx 150–350 µm in diameter) and the presence of CAFs in the tumor models. The latter can

www.advancedsciencenews.com



16136289,0, Downloaded from https://onlinelibrary.wiley.com/doi/10.1002/smll.202307355 by Wuhan University, Wiley Online Library on [28/11/2023]. See the Terms and Conditions (https://onlinelibrary.wiley.com/rems-and-conditions) on Wiley Online Library for rules of use; OA articles are governed by the applicable Creative Commons License

www.small-journal.com

increase the drug-resistance of MDA-MB-231 cells to anti-cancer therapeutics through soluble and secretory factor-mediated drug resistance and cell adhesion-mediated drug resistance.^[52]

By including endothelial cell-laden MiMS into the assembled co-culture, it had demonstrated the possibility of forming the tumor model with a vascular-like network (Figure 7), allowing for testing those anti-vascular drugs, which target endothelial cells for action rather than cancer cells, and eventually lead to cancer destruction.^[53] Thus, Cediranib, a small molecule inhibitor for VEGF receptors, [54] was tested for its anti-vascular efficacy with our vascularized tumor models composed of MDA-MB-231laden MaMS, NHDF-laden MaMS and EA.hy926 (human endothelial cells)-laden MiMS. Upon treated with 1 µM Cediranib for 48 h, the culture was immunofluorescently stained for CD31 to determine the anti-vascular efficacy. Apparently, the treated culture had fewer CD31-positive cells and noticeably lower endothelial sprouting/branching compared to non-treated controls (Figure 8C). Cediranib would not cause the death of endothelial cells, however, the angiogenesis was inhibited. Further analyses of the images revealed Cediranib treatment caused ≈50% reduction of the CD31-positive cells (Figure 8D). Measuring cell proliferation in the cultures without or with Cediranib treatment by Cell TiterBlue-based assay showed 31.89 \pm 0.06% reduction in the treated group (Figure 8E), consistent with the findings from clinical trials.^[54] Taken together, both studies confirmed the applicability of the tumor models for drug evaluation.

3. Conclusion

In recognition of the remaining unmet need for pathophysiologically relevant in vitro tumor models, the current study has explored the use of various porous PLGA microspheres as carriers to lade with selected cells (cancer, fibroblast and endothelial cells). Such cell-laden microspheres can be used as modules and further assembled into 3D constructs within a customized culture platform to form tumor tissue models with a spatial control of cell distribution and the formation of vascular-like network. Evidently, this microsphere-enabled modular strategy could at least partially recapture the complex cell organization of native tumor tissues and offer a flexible platform to create tissue mimetics with heterogeneous cells. Testing two known drugs (i.e., doxorubicin and Cediranib) on such models demonstrated their potential utility for drug evaluation. With increasing interest in "personalized medicine" for cancer therapies considering varying patient responses to therapeutics, tumor models we developed can be readily established with the cells isolated from patients. Testing available therapeutics on such in vitro tissue models would offer the most cost-effective treatment options to the patients in a short time frame. Clearly, with the capability of modulating the microsphere morphology, cell composition and spatial distribution, microsphere-enabled 3D tumor tissue formation offers a high flexibility to satisfy the needs for pathophysiological study, anticancer drug screening or design of personalized treatment.

4. Experimental Section

Materials: PLGA (85:15 ester terminated Mw: 50 000-75 000), ammonium bicarbonate, sodium hydroxide and poly vinyl alcohol (PVA)

(87%–90% hydrolyzed, average Mw: 30 000-70 000) were purchased from Sigma–Aldrich (St. Louis, MO). Doxorubicin (hydrochloride), and Cediranib were purchased from Cayman Chemical (Ann Arbor, MI). Dichloromethane (DCM) was acquired from Pharmco-Aaper (Brookfield, CO). MDA-MB-231 a mammary breast cancer cell line derived from pleural effusion, primary normal human dermal fibroblasts (NHDF, passage 4), human endothelial EA.hy926 cells, and MS-1 cells, an endothelial cell line from mouse, were all obtained from the American Type Culture Collection (ATCC, Manassas, VA). All other chemicals were used as received without further treatment.

Fabrication of Porous PLGA Microspheres: Porous PLGA microspheres were prepared via the water-in-oil-in-water (W1-O-W2) double emulsion^[55,56] with assistance of a customized microfluidic device to better control the microsphere diameter. Briefly, the water-in-oil solution as the discontinuous phase was prepared by mixing the saturated ammonium bicarbonate aqueous solution with the 1.5% (w/v) PLGA in DCM solution at a ratio of 1:3. This mixture was then transferred to a 3-mL syringe with a 25G needle. The needle tip was inserted into a low-density polyethylene (LDPE) tube (ID: 0.58 mm; OD: 0.99 mm) connected to another 10mL syringe contains 1% (w/v) PVA aqueous solution as the continuous phase. The discontinuous phase was pumped at a rate of 10 mL h^{-1} while the continuous phase was pumped at a rate of 1 mL min⁻¹. The mixture was then injected through the LDPE tube into a spinner flask containing 1% (w/v) PVA aqueous solution under continuous stirring (300 rpm). The system temperature was maintained above 30 °C to assure immediate decomposition of ammonium bicarbonate into gas (i.e., ammonia and carbon dioxide) and subsequently generate the pores within the PLGA microspheres. The solution was continuously stirred within the flask for 4 h at room temperature in order to enable DCM evaporation out of the microspheres. The final microspheres were collected by centrifugation and washed with deionized water for several times. To further modulate the mesopores of the PLGA microsphere surface, the microspheres were treated with ethanolic sodium hydroxide (NaOH) (30% 0.25 M NaOH and 70% absolute ethanol) for different durations. As a result, two major kinds of microspheres were accordingly prepared and used in this research, i.e., macroporous microspheres (MaMS, average surface pore size is larger than 20 µm) and microporous microspheres (MiMS, average surface pore size was $\approx 12 \, \mu \text{m}$).

Scanning Electron Microscopy: The morphology of as-prepared microspheres was examined with scanning electron microscopy (SEM) (Zeiss Auriga FIB-SEM with Leica VCT-100 cryo-system, Oberkochen, Germany). Briefly, air-dried microspheres were attached onto the SEM stages with double-sided adhesive tape, and then sputter-coated with gold for 1 min. SEM micrographs were acquired at 3.00 kV. At least five randomly selected SEM images were acquired for each type of microspheres, and images were manually analyzed using ImageJ software v1.5 (NIH, Maryland, US) to calculate the average microsphere diameter and pore size.

Micro-Computed Tomography (Micro-CT) Evaluation: After tension-free drying, the microspheres were set for the Micro-CT examination. The analysis was conducted using a Micro-CT imaging system Bruker SkyScan 1272 (Allentown, PA) to analyze the interior structure of microspheres following the standard protocols. The scanning conditions were: 50 kv-70 mu A, no filter, with a spatial resolution of 3 µm. The obtained data were reconstructed by NRecon (Version: 1.7.1.6) software. Analysis of the region of interest (ROI) was selected by CTAn (Version: 1.17.9.0) software. Pore size and porosity were obtained.

Cell Culture: Human breast carcinoma MDA-MB-231 cells, human endothelial EA.hy926 cells and mouse endothelial MS-1 cells were cultured in Dulbecco's Modified Eagle Medium (DMEM) with high glucose (4.5 g L $^{-1}$) supplemented with 10% fetal bovine serum (FBS), 100 IU mL $^{-1}$ penicillin and 100 mg mL $^{-1}$ streptomycin. NHDF cells were cultured in DMEM with low glucose (1 g L $^{-1}$) supplemented with 10% FBS, 100 IU mL $^{-1}$ penicillin and 100 mg mL $^{-1}$ streptomycin. Cells were incubated at 37 °C in a 90% humidified atmosphere of 5% CO $_2$. When cells reached 60%–70% confluence, they were subcultured at a 1-to-3 split ratio.

Dynamic Cell Seeding and Culture within the Spinner Flask: To assure maximum and evenly cell distribution among microspheres, MDA-MB-231 cells, NHDF cells, MS-1 cells and EA.hy926 cells were dynamically

www.small-journal.com

16136289,0, Downloaded from https://onlinelibrary.wiley.com/doi/10.1002/smll.202307355 by Wuhan University, Wiley Online Library on [28/11/2023]. See the Terms and Conditions (https://onlinelibrary.wiley.com/rems-and-conditions) on Wiley Online Library for rules of use; OA articles are governed by the applicable Creative Commons License

seeded onto the respective microspheres within the 100-mL spinner flasks. Briefly, cell suspension (4000 cell mL^{-1}) of individual cells was added into the respective spinner flasks containing 3000 microspheres (MaMS for MDA-MB-231 or NHDF; MiMS for MS-1 or EA.hy926) in 50 mL media. The spinner flasks were accommodated in a 37 °C incubator with 90% humidity and 5% CO₂ under the continuous stirring at the optimal speed (see Figure 3A). After 24 h, either cell-laden MaMS or MiMS were collected by gentle centrifugation at 1000 rpm and then individually resuspended in the DMEM media. The microspheres laden with corresponding cells were mixed at designated ratios and transferred into the customized microfluidic culture devices (as described below) for further 3D tissue formation.

Live/Dead Cell Staining: The cell viability cultured on different microspheres was examined with a Live/Dead Viability/Cytotoxicity kit (Molecular Probes, Invitrogen) according to the manufacturer's protocol. Briefly, cell-laden microspheres after 3-day culture were incubated with 2 μ M calcein acetoxymethyl ester (Calcein AM) and 0.5 µM ethidium homodimer-1 (EthD-1) for 30 min. Viable cells were fluorescently stained in green by Calcein AM whereas the nuclei of dead cells were fluorescently stained in red by EthD-1 as a result of membranolysis. The staining was examined with a Nikon Eclipse 80i epifluorescent microscope, and representative fluorescent images were digitally documented.

Microfluidic Device Fabrication and 3D Tissue Culture: In view of the many existing microfluidic culture systems, [57-61] which could accommodate multiple chambers but with only one inlet and one outlet. Upon growth of cells into 3D tissues, the shear stress built up around the inlet and outlet would induce unwanted cell death in that region. Meanwhile, the current microfluidic culture platforms are not designed for modular scaffolds as described hereafter. To address the above challenges, it was therefore designed the culture device with several unique attributes (see Figure 4A), comprising a media flow chamber and a culture chamber for cell-laden microspheres, compartmented by a media-permeable nylon mesh. The media chamber (150 µm in depth) enabled continuous media flow to provide oxygen and nutrients to the culture chamber through the nylon mesh similar to the arterioles. The nylon mesh with the pore size of 70 µm allowed free mass exchange while preventing the escape of cell-laden microspheres into the media chamber. The designed devices were fabricated with the aid of a 3D printed mold. Briefly, the molds for media and culture chambers were first printed with a 3D printer (X-One Qidi Tech, Zhejiang, China) as designed. Polydimethylsiloxane (PDMS) was then poured onto the molds to form the chambers. An inlet and outlet $(\phi = 300 \mu m)$ were made to the media chamber with a punch. Pressure sensitive adhesive double-sided tape was applied to the surfaces for assembly. Then all the parts were sterilized with 70% (v/v) isopropanol for 30 min, air-dried and then irradiated for another 30 min with UV. Cell-laden microspheres were then transferred into the culture chamber prior to its assembly with other parts for culture. Either single or mixed media (1:1, v/v) was introduced through the inlet to the culture devices at a flow rate of 2.5 μL min⁻¹.

Morphological and Histological Analyses: Microfluidic-cultured tissue samples were harvested at designated time points for analyses. To assure tissue integrity, 4% (w/v) paraformaldehyde (PFA) in phosphate buffered saline (PBS) solution was slowly injected into the microfluidic device and left for incubation for 1 h. After fixation, a surgical scalpel was used to separate and detach the tissue culture chamber. The cultured samples were carefully cut into half. One half was used for histological staining and the other half was used for immunofluorescence staining. 10-day cultured samples were also stained with 1% methylene blue for structural integrity confirmation. For histological staining, tissue samples were dehydrated in a series of graded ethanol and then embedded in glycol methacrylate (GMA). Thin cross-sections (5 μm) were cut and stained with hematoxylin and eosin (H&E) for cell distribution and tissue formation. The stained slides were examined under a Nikon light microscope, and representative images were digitally documented. For immunofluorescence staining, tissue samples were respectively incubated in 15% (v/v) and 30% (v/v) sucrose in PBS and embedded in the optimal cutting temperature (O.C.T.) compound. The specimens were sectioned into 6-µm-thick slices with the cryostat microtome. The slices were permeabilized with 0.1% (w/v) Triton X-100 in PBS and blocked with 3% (w/v) BSA in PBS. Afterwards, slices were incubated with PECAM-1 (MEC 13.3, 1:200) primary antibody for 1 h and subsequently incubated with fluorescein (FITC)-conjugated AffiniPure goat anti-rat IgG(H+L) (1:200) for 1 h. Cell nuclei were stained with DAPI (Sigma, 1:1000). The staining was examined under a Nikon Eclipse 80i epifluorescence microscope and representative images were digitally documented. For methylene blue staining, samples fixed with 4% (w/v) PFA were incubated with 1% (w/v) methylene blue solution for 20 min and then washed with deionized water 3 times. The stained samples were then examined under a Nikon SMZ1500 stereomicroscope and representative images were digitally documented.

Drug Treatment to Cultured Tissue within Microfluidic Chambers: Drug stock solutions of doxorubicin (hydrochloride) and Cediranib were prepared by dissolving in dimethyl sulfoxide (DMSO) and aliquoted for storage at -20 °C. The drug stock solutions were diluted with fresh media with a final DMSO concentration <0.1% (v/v) before use. The diluted doxorubicin with a final concentration of (2, 3, and 4 µM) was pumped into the microfluidic chambers containing NHDF- and cancer cell-laden MaMS (1:2) for 48 h. The diluted Cediranib with a final concentration of $1 \mu M$ was pumped into the microfluidic chambers containing the coculture of human endothelial cell-laden MiMS, cancer cell-laden MaMS and fibroblastladen MaMS for 48 h

CellTiter-Blue Cell Viability Assay: The CellTiter-Blue Cell Viability Assay, which relies on a fluorometric indicator dye resazurin to measure the metabolic activities of cells, can be used to quantitatively estimate the number of viable cells. Thus, the viable cells present in the tissue before and after drug treatments were evaluated with the CellTiter-Blue Cell Viability Assay kit (Promega) according to the manufacturer's protocol. Briefly, the CellTiter-Blue working solution was diluted to a final concentration of 20% (v/v) with fresh media right before each experiment and then injected to the microfluidic chambers containing tissues and incubated for 4 h. During the incubation, dark blue and non-fluorescent resazurin was reduced to the pink and highly fluorescent resorufin by viable cells. The reduced CellTiter-Blue solution was then collected, and the fluorescence intensity was recorded with the multi-detection microplate reader (BioTek Instruments Inc., Winooski, VT) under the wavelength 560Ex/590Em.

Zombie Aqua Fixable Viability Assay: The cell viability within the 3D tissue upon various drug treatments was also determined with the Zombie Aqua fixable viability assay (BioLegend) according to the manufacturer's protocol. Briefly, the diluted stock staining solution (1:100 with PBS) was infiltrated through the microfluidic chambers for 30 min. The stained tissue was washed twice with 1% (w/v) BSA aqueous solution, fixed with 4% PFA for overnight and then embedded in the O.C.T. compound. The specimens were sectioned into thin slices and then examined under a Nikon Eclipse 80i epifluorescence microscope. Only dead cells before fixation would show the bright green fluorescence.

Statistical Analysis: All the data above were presented as mean ± standard deviation and evaluated by the T-test and one-way ANOVA test. The results were considered statistically significant with a p-value less than

Supporting Information

Supporting Information is available from the Wiley Online Library or from the author.

Acknowledgements

W. W. and L. Z. contributed equally to this work. This study was financially supported by National Science Foundation (NSF-DMR award number 1508511 and NSF-GCR award number 2219014), and NIAMS award number 1R01AR067859. The authors were grateful for the scientific input from Dr. Marcin Iwanicki (Stevens Institute of Technology).

Conflict of Interest

The authors declare no conflict of interest.

16136829, 0, Downloaded from https://onlinelibrary.wiley.com/doi/10.1002/smll.102.307365 by Wuhan University, Wiley Online Library on [28/11/2023]. See the Terms and Conditions (https://onlinelibrary.wiley.com/terms-and-conditions) on Wiley Online Library for rules of use; OA articles are governed by the applicable Creative Commons

Data Availability Statement

The data that support the findings of this study are available on request from the corresponding author. The data are not publicly available due to privacy or ethical restrictions.

Keywords

anticancer drug screening, in vitro tumor model, microspheres, modular tissue formation, vascularization

> Received: October 1, 2023 Published online:

- [1] BREASTCANCER.ORG, U. S., Breast Cancer Statistics 2018.
- [2] M. J. Engstrøm, S. Opdahl, A. I. Hagen, P. R. Romundstad, L. A. Akslen, O. A. Haugen, L. J. Vatten, A. M. Bofin, Breast Cancer Res. Treat. 2013, 140, 463.
- [3] D. Cook, D. Brown, R. Alexander, R. March, P. Morgan, G. Satterthwaite, M. N. Pangalos, Nat. Rev. Drug Discov. 2014, 13, 419.
- [4] C. Fischbach, R. Chen, T. Matsumoto, T. Schmelzle, J. S. Brugge, P. J. Polverini, D. J. Mooney, Nat. Methods 2007, 4, 855.
- [5] F. Pampaloni, E. G. Reynaud, E. H. K. Stelzer, Nat. Rev. Mol. Cell Biol. 2007. 8. 839.
- [6] C. L. Morton, P. J. Houghton, Nat. Protoc. 2007, 2, 247.
- [7] C. Lovitt, T. Shelper, V. Avery, Biology 2014, 3, 345.
- [8] L. David, V. Dulong, D. Le Cerf, L. Cazin, M. Lamacz, J.-P. Vannier, Acta Biomater. 2008, 4, 256.
- [9] S.-W. Kang, Y. H. Bae, Biomaterials 2009, 30, 4227.
- [10] L. Ma, C. Zhou, B. Lin, W. Li, Biomed. Microdevices 2010, 12, 753.
- [11] S. Moon, S. K. Hasan, Y. S. Song, F. Xu, H. O. Keles, F. Manzur, S. Mikkilineni, J. W. Hong, J. Nagatomi, E. Haeggstrom, A. Khademhosseini, U. Demirci, Tissue Eng Part C Methods 2010, 16,
- [12] A. Skardal, J. Zhang, L. Mccoard, X. Xu, S. Oottamasathien, G. D. Prestwich, Tissue Eng Part A 2010, 16, 2675.
- [13] J. Folkman, N. Engl. J. Med. 1971, 285, 1182.
- [14] J. Folkman, R. Kalluri, Nature 2004, 427, 787.
- [15] M. A. Gimbrone, S. B. Leapman, R. S. Cotran, J. Folkman, J. Exp. Med. 1972, 136, 261.
- [16] M. Cobleigh, Semin. Oncol. 2003, 30, 117.
- [17] J. C. Yang, L. Haworth, R. M. Sherry, P. Hwu, D. J. Schwartzentruber, S. L. Topalian, S. M. Steinberg, H. X. Chen, S. A. Rosenberg, N. Engl. I. Med. 2003, 349, 427.
- [18] R. J. Mayer, N. Engl. J. Med. 2004, 350, 2406.
- [19] H. Hurwitz, L. Fehrenbacher, W. Novotny, T. Cartwright, J. Hainsworth, W. Heim, J. Berlin, A. Baron, S. Griffing, E. Holmgren, N. Ferrara, G. Fyfe, B. Rogers, R. Ross, F. Kabbinavar, N. Engl. J. Med. 2004, 350, 2335.
- [20] A. S. Timin, O. O. Peltek, M. V. Zyuzin, A. R. Muslimov, T. E. Karpov, O. S. Epifanovskaya, A. I. Shakirova, M. V. Zhukov, Y. V. Tarakanchikova, K. V. Lepik, V. S. Sergeev, G. B. Sukhorukov, B. V. Afanasyev, ACS Appl. Mater. Interfaces 2019, 11, 13091.
- [21] A. R. Muslimov, A. S. Timin, V. R. Bichaykina, O. O. Peltek, T. E. Karpov, A. Dubavik, A. Nominé, J. Ghanbaja, G. B. Sukhorukov, M. V. Zyuzin, Biomater. Sci. 2020, 8, 1137.
- [22] T. Okudaira, N. Amimoto, H. Mizumoto, T. Kajiwara, J. Biosci. Bioeng. 2016, 122, 213.
- [23] L. Rossi, C. Attanasio, E. Vilardi, M. De Gregorio, P. A. Netti, J. Mater. Sci. Mater. Med. 2016, 27, 107.

- [24] Y. Zhou, H.-L. Gao, L.-L. Shen, Z. Pan, L.-B. Mao, T. Wu, J.-C. He, D.-H. Zou, Z.-Y. Zhang, S.-H. Yu, Nanoscale 2016, 8, 309.
- [25] B. S. Schon, G. J. Hooper, T. B. F. Woodfield, Ann. Biomed. Eng. 2017, 45, 100.
- [26] F. Perche, V. P. Torchilin, Cancer Biol. Ther. 2012, 13, 1205.
- [27] B. J. Lawrence, S. V. Madihally, Cell Adh. Migr. 2008, 2, 9.
- [28] H. K. Kim, H. J. Chung, T. G. Park, J. Control Release 2006, 112, 167.
- [29] O. Qutachi, J. R. Vetsch, D. Gill, H. Cox, D. J. Scurr, S. Hofmann, R. Müller, R. A. Quirk, K. M. Shakesheff, C. V. Rahman, Acta Biomater. 2014, 10, 5090.
- [30] G. Q. Teixeira, C. C. Barrias, A. H. Lourenço, R. M. Gonçalves, Tissue Eng Part C Methods 2014, 20, 984.
- [31] T.-W. Chung, D.-Z. Liu, S.-Y. Wang, S.-S. Wang, Biomaterials 2003, 24, 4655.
- [32] G. Rijal, W. Li, Sci. Adv. 2017, 3, e1700764.
- [33] Y. K. Girard, C. Wang, S. Ravi, M. C. Howell, J. Mallela, M. Alibrahim, R. Green, G. Hellermann, S. S. Mohapatra, S. Mohapatra, PLoS One 2013, 8, e75345.
- [34] W. Li, Z. Zhou, X. Zhou, B. L. Khoo, R. Gunawan, Y. R. Chin, M. Yang, Adv. Healthc. Mater. 2023, e2202609.
- [35] C. T. Mierke, J. Biophys. 2008, 183516.
- [36] G. L. Nicolson, EXS 1995, 74, 123.
- [37] C. Han, T. Liu, R. Yin, Biomark. Res. 2020, 8, 64.
- [38] F. Xing, Front. Biosci. (Landmark Ed) 2010, 15, 166.
- [39] A. M. Mendonsa, T.-Y. Na, B. M. Gumbiner, Oncogene 2018, 37, 4769.
- [40] S. P. S. Dhami, S. Patmore, C. Comerford, C. M. Byrne, B. Cavanagh, I. Castle, C. C. Kirwan, M. Kenny, I. Schoen, J. S. O'donnell, J. M. O'sullivan, J. Thromb. Haemost. 2022, 20, 2350.
- [41] R. F. Potter, A. C. Groom, Microvasc. Res. 1983, 25, 68.
- [42] G. Vilanova, I. Colominas, H. Gomez, Int. J. Numer. Method Biomed. Eng. 2013, 29, 1015.
- [43] G. P. Gupta, J. Massagué, Cell 2006, 127, 679.
- [44] P. S. Steeg, Nat. Med. 2006, 12, 895.
- [45] N. G. Huilgol, M. M. Khan, R. Puniyani, Indian J. Cancer 1995, 32, 59.
- [46] R. Montironi, L. Diamanti, D. Thompson, H. G. Bartels, P. H. Bartels, Eur. Urol. 1996, 30, 191.
- [47] M. J. Siemerink, M. R. Hughes, M. G. Dallinga, T. Gora, J. Cait, I. M. C. Vogels, B. Yetin-Arik, C. J. F. Van Noorden, I. Klaassen, K. M. Mcnagny, R. O. Schlingemann, PLoS One 2016, 11, e0157902.
- [48] S. Rivankar, J. Cancer Res. Ther. 2014, 10, 853.
- [49] D. Carlisi, A. De Blasio, R. Drago-Ferrante, R. Di Fiore, G. Buttitta, M. Morreale, C. Scerri, R. Vento, G. Tesoriere, Cell Death Discov. 2017, 3, 17078.
- [50] L. Florento, R. Matias, E. Tuano, K. Santiago, F. Cruz, A. Tuazon, Int. I. Biomed. Sci. 2012, 8, 76.
- [51] C. J. Lovitt, T. B. Shelper, V. M. Avery, BMC Cancer 2018, 18, 41.
- [52] M. B. Meads, R. A. Gatenby, W. S. Dalton, Nat. Rev. Cancer 2009, 9,
- [53] A. J. Hayes, West J. Med. 2000, 172, 39.
- [54] U. A. Matulonis, S. Berlin, P. Ivy, K. Tyburski, C. Krasner, C. Zarwan, A. Berkenblit, S. Campos, N. Horowitz, S. A. Cannistra, H. Lee, J. Lee, M. Roche, M. Hill, C. Whalen, L. Sullivan, C. Tran, B. D. Humphreys, R. T. Penson, J. Clin. Oncol. 2009, 27, 5601.
- [55] S.-W. Choi, Y. Zhang, Y. Xia, Adv. Funct. Mater. 2009, 19, 2943.
- [56] S.-W. Choi, Y.-C. Yeh, Y. Zhang, H.-W. Sung, Y. Xia, Small 2010, 6, 1492.
- [57] P. T. Charles, J. Davis, A. A. Adams, G. P. Anderson, J. L. Liu, J. R. Deschamps, A. W. Kusterbeck, Talanta 2015, 144, 439.
- [58] K. C. Chaw, M. Manimaran, F. E. H. Tay, S. Swaminathan, Microvasc. Res. 2006, 72, 153.
- [59] K.-J. Jang, K.-Y. Suh, Lab Chip 2010, 10, 36.
- [60] X. Pan, L. Jiang, K. Liu, B. Lin, J. Qin, Anal. Chim. Acta 2010, 674, 110.
- [61] W. Yu, H. Qu, G. Hu, Q. Zhang, K. Song, H. Guan, T. Liu, J. Qin, PLoS One 2014, 9, 89966.